

# Electrochemical Metallization Memristive Devices with Al Active Electrode Using Engineered Mixed Hexagonal/Orthorhombic Polycrystalline YMnO<sub>3</sub>

Rong Wu, Sebastian W. Schmitt, Florian Maudet, Dong Jik Kim, Veeresh Deshpande, and Catherine Dubourdieu\*

We report electrochemical metallization (ECM) resistive switching in polycrystalline YMnO<sub>3</sub> memristive devices using Al as an active electrode. Al/YMnO<sub>3</sub>/Pt devices exhibit bipolar resistive switching with a high  $R_{\text{OFF}}/R_{\text{ON}}$  ratio of  $10^4$ , low operational voltages of  $V_{\text{Set}} \approx 1.7$  V and  $V_{\text{Reset}} \approx -0.36$  V and good retention properties. The resistive switching is intimately linked to the coexistence of the orthorhombic and hexagonal YMnO<sub>3</sub> phases. The characterization of these two nanocrystalline phases is realized not only by X-ray diffraction – which is shown to be unable to reveal the presence of the orthorhombic phase – but also by a set of correlative microscopy and spectroscopy methods (scanning electron microscopy, optical microscopy, Raman spectroscopy and conductive atomic force microscopy). The origin of resistive switching is ascribed to an Al filament-based electrochemical metallization mechanism that likely occurs along an oxygen-deficient grain boundary between the hexagonal and orthorhombic nanocrystalline YMnO<sub>3</sub> phases. The unique microstructure provided by the mixed polycrystalline phase films allows to use Al as an active electrode in YMnO<sub>3</sub>-based ECM cells, and gives perspective for further miniaturization of the devices.

structure with space group  $P6_3cm$  for the smaller rare earths ( $R = \text{Sc, Y, Ho to Lu}$ ) and a distorted orthorhombic one with space group  $Pbnm$  for the larger rare earths ( $\text{La to Dy}$ ).<sup>[1]</sup> Due to their remarkable multi-ferroic properties - ferroelectricity at room temperature and anti-ferromagnetism at temperatures typically below  $\approx 100$  K<sup>[2]</sup> - hexagonal RMnO<sub>3</sub> have been widely studied in the last 2 decades. They exhibit a very peculiar ferroelectric domain structure with a “cloverleaf” like shape, where six domains merge at a single line defect, which originates from a geometrically-driven structural phase transition.<sup>[3,4]</sup>

Recently, resistive switching behavior has been demonstrated in polycrystalline hexagonal YMnO<sub>3</sub> (h-YMO) thin films with promising applications for neuromorphic devices.<sup>[5–10]</sup> Combining resistive switching properties together with ferroelectricity could offer in a long term promising avenues for the development of multistate analog devices.

## 1. Introduction

Rare-earth manganites (RMnO<sub>3</sub>) crystallize in two different crystalline structures at ambient conditions depending on the ionic radius of the rare earth element: a hexagonal crystal

Different electrodes, YMO composition/microstructure and different mechanisms have been reported for YMO-based memristive devices. Yan et al. reported unipolar resistive switching in Pt/YMn<sub>1– $\delta$</sub> O<sub>3</sub>/Pt stacks.<sup>[5]</sup> The resistive switching behavior was explained by the formation and rupture of conductive filaments induced by Mn vacancies. Later, Bogusz et al. investigated unipolar resistive switching of h-YMO films sandwiched between Au or Al top and Pt bottom electrodes, and reported oxygen vacancies to be responsible for the formation of conductive filaments along grain boundaries and charged domain walls.<sup>[6,7]</sup> Wei et al. observed multilevel bipolar resistive switching in In/YMO/Nb:SrTiO<sub>3</sub> devices, which was explained by the modification of the depletion region at the pn junction interface between h-YMO and Nb:SrTiO<sub>3</sub> upon polarization reversal.<sup>[8]</sup> Furthermore, cations doped h-YMO was recently studied by Rayapati et al. for electroforming-free filamentary unipolar resistive switching in Al/h-YMO/Pt stacks<sup>[9]</sup> and by K. N. Rathod et al. for interface-type bipolar resistive switching in Ag/h-YMO/Si.<sup>[10]</sup> Studies have been so far focused on polycrystalline hexagonal YMO thin films (stoichiometric and off-stoichiometric YMO) with different bottom and top electrodes. However, given the challenges associated with achieving single-phase polycrystalline

R. Wu, S. W. Schmitt, F. Maudet, D. J. Kim, V. Deshpande, C. Dubourdieu  
Institute Functional Oxides for Energy-Efficient Information Technology  
Helmholtz-Zentrum Berlin für Materialien und Energie  
Hahn-Meitner Platz 1, 14109 Berlin, Germany  
E-mail: catherine.dubourdieu@helmholtz-berlin.de

R. Wu, C. Dubourdieu  
Physical and Theoretical Chemistry  
Freie Universität Berlin  
Arnimallee 22, 14195 Berlin, Germany

 The ORCID identification number(s) for the author(s) of this article can be found under <https://doi.org/10.1002/sstr.202300494>.

© 2024 The Authors. Small Structures published by Wiley-VCH GmbH. This is an open access article under the terms of the Creative Commons Attribution License, which permits use, distribution and reproduction in any medium, provided the original work is properly cited.

DOI: 10.1002/sstr.202300494

h-YMO thin films<sup>[11–15]</sup> and considering that X-ray diffraction may not provide conclusive evidence for the absence of orthorhombic YMnO<sub>3</sub> phase (o-YMO) - as we will show later - it is plausible that the reported resistive switching performances could be influenced by contributions from both crystalline phases. Moreover, all reported devices mentioned above can be classified as valence change memory devices, involving either a filamentary or an interfacial mechanism.<sup>[16]</sup> No electrochemical metallization memory has been so far reported with YMO.

In this work, we investigate Al/YMO/Pt memristive devices with polycrystalline YMO films containing a mixture of o-YMO and h-YMO phases engineered via the annealing conditions of amorphous YMO. The presence of secondary o-YMO with respect to h-YMO is clearly evidenced combining optical microscopy, scanning electron microscopy (SEM), Raman spectroscopy and conductive atomic force microscopy (c-AFM). In contrast to previous studies reporting unipolar resistive switching in polycrystalline YMO-based devices with Pt bottom and Al top electrodes,<sup>[6,7,9]</sup> we show an electroforming-free bipolar resistive switching behavior, with remarkable low operational voltages (Set and Reset voltages of  $\approx 1.7$  and  $\approx -0.36$  V respectively). The resistive switching is attributed to an electrochemical metallization mechanism with the formation of Al filaments likely occurring along oxygen-deficient grain boundaries between the hexagonal YMO phase and the secondary orthorhombic YMO phase.

## 2. Results and Discussion

### 2.1. Characterization and Control of Hexagonal and Orthorhombic Crystalline Phases

The grazing incidence X-ray diffraction (GIXRD) patterns of the as-deposited film (noted A) and annealed films (at 725, 800 and 900 °C under N<sub>2</sub> for 30 min) are shown in **Figure 1a**. The as-deposited film is amorphous; only the peaks from the Pt thin film appear.<sup>[17]</sup> At 725 °C the films crystallize mainly in the hexagonal phase<sup>[18]</sup> but a few peaks from the orthorhombic phase<sup>[19]</sup> also appear (Figure 1a). These peaks are no more observed for the samples annealed at 800 and 900 °C. However, we will show later, using other techniques, that the orthorhombic phase is still present.

The calculation of the free energy of RMnO<sub>3</sub> formation from R<sub>2</sub>O<sub>3</sub> and Mn<sub>2</sub>O<sub>3</sub> at 900 °C<sup>[20]</sup> (calculated using oxygen dissociation pressure data<sup>[21]</sup>) shows that there is only a small difference for YMnO<sub>3</sub> between the thermodynamically stable hexagonal and the metastable orthorhombic phases. As a consequence, the metastable orthorhombic phase of YMO can be stabilized under certain conditions, such as high pressure synthesis,<sup>[22–25]</sup> soft chemistry synthesis<sup>[26,27]</sup> and, as thin films, by epitaxial strain.<sup>[28,29]</sup> In polycrystalline thin films, Romaguera-Barcelay et al. reported the persistence of o-YMO phase in h-YMO films prepared on Si/SiO<sub>2</sub>/Ti/Pt substrates by chemical solution deposition and annealed at 875 °C. They concluded that the presence

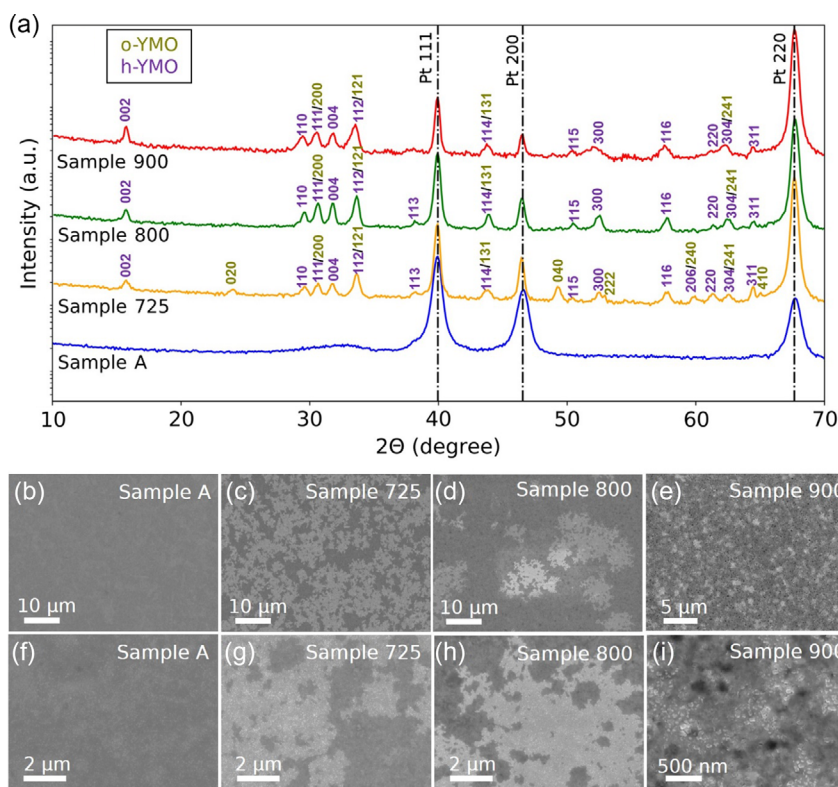


**Figure 1.** a) GIXRD patterns of samples A (as-deposited amorphous film), 725 (film annealed at 725 °C), 800 (film annealed at 800 °C), and 900 (film annealed at 900 °C) deposited on Pt/Ti/SiO<sub>2</sub>/Si substrates. Reflections indexed in green and purple are attributed to o-YMO and h-YMO phases, respectively. b–i) SEM images of samples (b,f) A, (c,g) 725, (d,h) 800, and (e,i) 900. All annealings were performed under N<sub>2</sub> for 30 min.

of o-YMO was associated with the induced strain from the substrate.<sup>[15]</sup> Similarly, the presence of the orthorhombic phase in our films might be due to the strain originating from the strong mismatch of the lattice expansion coefficients between YMO and the Pt metal substrate.

The crystallization of the h-YMO phase from the amorphous phase at atmospheric pressure requires a quite high temperature of 800 °C in case of ceramics,<sup>[30,31]</sup> while the films can be crystallized at 725 °C in this work. The estimated lattice parameters of h-YMO in the different samples are presented in **Table 1** and compared to those of single crystals.<sup>[18]</sup> We observed that both *a* and *c* lattice parameters in the films are significantly smaller than the ones of single crystals prepared at atmospheric pressure. In powders, the crystal structure of h-YMO nanocrystallites smaller than 80 nm has been shown to deviate from the bulk material in terms of unit cell distortion and unit cell volume.<sup>[30]</sup> However, the expected lattice parameters of YMO with grain sizes of 40 ± 15 nm (SEM data below) are much larger than our values.<sup>[30]</sup> An explanation of the relatively small *a* and *c* values is provided when comparing our data with the ones of single crystals prepared under 5 GPa (Table 1, ref. [18]). The good agreement between our values and those of high-pressure single crystals indicates that the strain imparted by the Pt substrate upon cooling from high temperature (725–900 °C) to room temperature results in an effect similar to that of high pressure.

After annealing, all films are quite rough, as shown by the AFM images in Figure S1, Supporting Information. Amorphous YMO films exhibit a rms roughness of ≈7 nm, slightly larger than the one of the starting Pt layer (≈4.9 nm). After annealing, the polycrystalline YMO films experience a strong increase in roughness, reaching a rms value of typically ≈14 nm (about 20% of the total thickness of 75 nm) for films annealed at 725 and 800 °C.

The SEM images of the four samples described above are shown in Figure 1b–i. The samples annealed at 725 and 800 °C exhibit a similar morphology, with regions of bright and dark contrasts (Figure 1c,g,d,h) and crystallites with grain sizes of 40 ± 15 nm. Optical microscope images of the same two films are shown in Figure S2b,c, Supporting Information. They also exhibit a contrast in which darker regions show similar features to the bright regions in the SEM images. Bright and dark contrast regions in low acceleration voltage (1.0 kV) SEM images of polycrystalline YMO thin films were also observed by Rayapati et al.<sup>[32]</sup> The authors explained them in terms of ferroelectric

domain imaging with the contrast originating from a variable secondary electron yield from ferroelectric charge domain density network.<sup>[32]</sup> For comparison, SEM images with a low acceleration voltage of 1.0 kV were also captured on our samples, as presented in Figure S3, Supporting Information. The images also show a bright and dark contrast pattern. In the following, we show that these dark and bright regions do not represent ferroelectric domains but are the signature of the two different YMO crystalline phases - orthorhombic and hexagonal.

Raman spectroscopy mapping was performed using the intensity of the A<sub>1</sub>(TO<sub>9</sub>) mode at 686 cm<sup>-1</sup> (scan size of 10 × 20 μm<sup>2</sup>, beam size of 1 μm, spatial resolution of ≈1 μm). This mode corresponds to the apical oxygen atoms (O1 and O2) stretching along the *c*-axis and is associated to the tilting and trimerization of the MnO<sub>5</sub> polyhedra in the hexagonal phase.<sup>[33]</sup> It is absent in the orthorhombic phase. The mapped region, indicated by the violet dashed box in the SEM image of **Figure 2a** (and in the optical image of Figure 2b) includes both regions of high and low SEM secondary electron yields (low and high brightness in optical microscopy). The Raman intensity map shown in Figure 2c presents two distinct regions colored in blue (“Region 1”) and red (“Region 2”), based on the intensity of the peak at 686 cm<sup>-1</sup>. A typical Raman spectrum for each of these two regions is shown in Figure 2d. The positions of the different peaks are listed in **Table 2** and compared to those of a single crystal. While the red curve indicates the presence of pure h-YMO, the blue one indicates the presence of o-YMO with a minor h-YMO contribution. Comparing the Raman map with Figure 2a,b shows that a high secondary electron yield in SEM and low brightness in optical microscopy is a signature of the o-YMO crystalline phase (“Region 1” colored in blue in Figure 2c). Vice versa, a low secondary electron yield in SEM and high brightness in optical microscopy is a signature of the h-YMO crystalline phase (“Region 2” colored in red in Figure 2c). Note that, as the bright features in the SEM images have irregular and “branched-like” shapes, each measured spot of size of 1 × 1 μm<sup>2</sup> might include small amounts of h-YMO, which explains why the mode at 686 cm<sup>-1</sup> is weakly detected in “Region 1”. Since the bright regions can also clearly be observed by optical microscopy (see Figure 2b), our results provide a quick and easy method to assess the presence of both phases in a film after its growth. The above observations prove the presence of the orthorhombic phase, which could not be determined from the GIXRD pattern of sample 800 (Figure 1a).

The presence of the orthorhombic phase in the hexagonal phase matrix is further confirmed by conductive AFM (c-AFM) measurements. It is indeed expected that both phases have significantly different conduction properties. The orthorhombic phase has been reported to have a higher electrical conductivity than that of the hexagonal phase.<sup>[34]</sup> The c-AFM spatial mapping shown in Figure 2e was performed in the black box area of Figure 2a,b. A direct correlation is observed between the highly conducting regions, the bright regions in the SEM image (Figure 2a), the dark regions in the optical microscopy image (Figure 2b), and the region identified as o-YMO in the Raman mapping (Figure 2c). The topography image in Figure 2f shows that there is no significant difference in the surface morphology between the high and low conductive regions. This finding matches the observation from the SEM images (Figure 1g,h),

**Table 1.** Lattice parameters and volume of unit cell of hexagonal phase in YMO films annealed at 725, 800 and 900 °C and of hexagonal single crystalline YMO from ref. [18] the 111 peak at  $2\theta = 40.05^\circ$  of Pt was taken as reference. The in-plane *a* and the out-of-plane *c* lattice parameters were calculated from the 110 and 004 peaks, respectively.

Samples	In-plane lattice <i>a</i> [Å]	Out-of-plane lattice <i>c</i> [Å]	Volume of cell [Å <sup>3</sup> ]
Single crystal (0 GPa) <sup>[18]</sup>	6.151	11.410	373.86
Single crystal (5 GPa) <sup>[18]</sup>	6.067	11.305	360.37
Sample 725	6.00	11.23	350.12
Sample 800	6.02	11.23	352.45
Sample 900	6.04	11.20	353.85

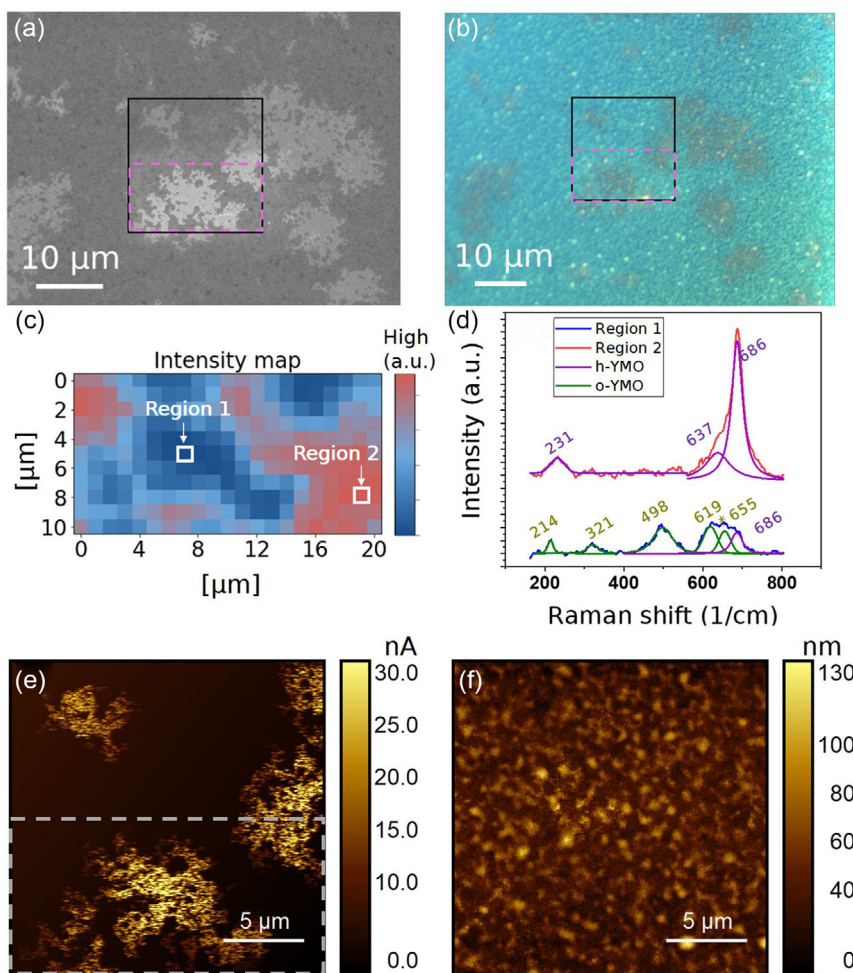


**Figure 2.** a) SEM and b) optical microscopy images of sample 800. The black and violet boxes correspond to the region of the c-AFM and Raman mapping, respectively. c) Map of the intensity of the mode  $A_1(TO_9)$  ( $686\text{ cm}^{-1}$ ) characteristic of the h-YMO phase. The map was recorded in the area marked by the violet dashed box in (a,b). d) Two Raman spectra representing “Region 1” (blue) and “Region 2” (red), marked with white boxes in (c). e) Current map measured with c-AFM in the area marked by the black box in (a,b). The grey rectangle indicates the location of the Raman map, shown in panel (c). f) Topography map recorded simultaneously with the c-AFM map in (e).

**Table 2.** Raman active modes and their wave number recorded on sample 800 and reported in literature.

Reported h-YMnO <sub>3</sub> [ $\text{cm}^{-1}$ ]			Reported o-YMnO <sub>3</sub> [ $\text{cm}^{-1}$ ]			Our work	
Mode	Calculated <sup>[33]</sup>	Measured <sup>[52]</sup>	Mode	Calculated <sup>[53]</sup>	Measured <sup>[53]</sup>	Region 1	Region 2
$E_2(5)$	243	215	$B_{2g}(5)$	162	220	214	
$E_1(TO_5)$	274	238	$A_g(6)$	304	323	$A_g(6)$ 321	$E_1(TO_5)$ 231
$E_1(TO_{14})$	644	632	$A_g(3)$	466	497	$A_g(3)$ 498	$E_1(TO_{14})$ 637
$A_1(TO_9)$	691	681	$B_{2g}(1)$	617	616	$B_{2g}(1)$ 619	$A_1(TO_9)$ 686
					653 <sup>a)</sup>	655 <sup>a)</sup>	
						$A_1(TO_9)$ 686	

<sup>a)</sup>This Raman shift is not related to a proper vibration mode from o-YMO<sup>[53]</sup>; it might be originating from defects<sup>[54]</sup> or contributions from zone-boundary phonons.<sup>[53]</sup>

where the film surface shows a homogenous granular appearance and excludes a topographic contribution to the contrast observed in the SEM images.

From these correlated microscopy and spectroscopy analyses, we clearly identify the presence of the orthorhombic phase in the polycrystalline hexagonal YMnO<sub>3</sub> films, which cannot be

determined by X-ray diffraction due to either low volume amount and nanosize grain leading to non-detectable peaks and/or the fact that several peaks of the hexagonal and orthorhombic phases overlap or are very close. We are also able to obtain quantitative information on the crystalline fraction – ratio of o-YMO to h-YMO - using processing algorithms of dark/bright regions in SEM images. Films annealed at 725 and 800 °C contain  $\approx 52\%$  and  $\approx 10\%$  o-YMO, respectively, as shown in Figure S4, Supporting Information. Since the secondary electron originate from the surface, these numbers do not represent a volume ratio.

The amount of the orthorhombic phase in the films decreases as the annealing temperature increases from 725 to 900 °C. At 900 °C, the microstructure changes significantly with pinholes appearing (Figure 1e,i). The Raman spectroscopy study shows that a small contribution of the orthorhombic phase is still present (Figure S5, Supporting Information). A higher temperature

would be necessary to crystallize pure hexagonal phase. However, as shown in Figure S6, Supporting Information, the films annealed at 1000 °C - exhibiting a larger grain size as compared to samples 725, 800 and 900 - have microcracks, which originate from the tensile stress induced by the thermal mismatch between the YMO film and the Pt coated substrate during the post annealing process upon cooling.<sup>[13,35]</sup> Moreover, due to the highly anisotropic thermal expansion coefficients of the h-YMO unit cell, stress is easily promoted.<sup>[13]</sup>

## 2.2. Bipolar Resistive Switching of Al/YMnO<sub>3</sub>/Pt Devices

Current–voltage (*I*–*V*) measurements were performed on the Al/YMO/Pt devices as illustrated in Figure 3a. The leakage current densities at 50 mV in the pristine state are presented in Figure 3b for the different devices as a function of the active area.

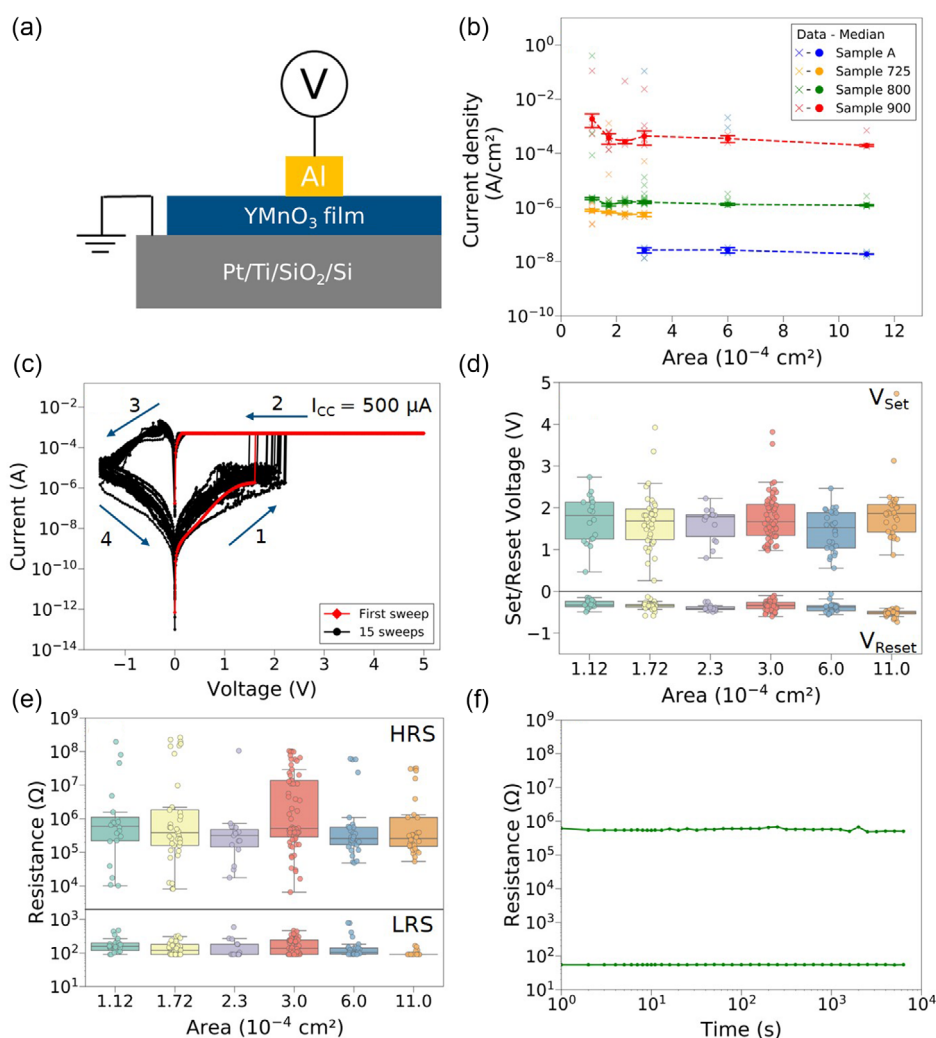


**Figure 3.** a) Sketch of the devices and applied bias. The Pt bottom electrode was grounded, and the DC voltage bias was applied to the top Al electrodes. b) Variation of the initial current density (pristine state) of the devices fabricated with samples annealed at 725, 800, and 900 °C for different device areas (read voltage of 50 mV). c–f) Characteristics of devices fabricated with a film annealed at 800 °C. (c) Typical *I*–*V* curves (15 cycles are shown). The *I*–*V* curve shown in red represents the first cycle. Variations of Set, Reset voltages (d) and resistances in the high (HRS) and low (LRS) resistance states (read voltage of 50 mV) (e) for different device areas. Three devices were measured for each device area. (f) Retention of HRS and LRS for one typical device (read voltage of 10 mV). For the box plots in (d) and (e), median values and their corresponding median absolute deviations are represented.

They are the smallest,  $\approx 10^{-8}$  A cm $^{-2}$ , for amorphous YMO. The devices prepared with YMO annealed at 900 °C exhibit a large leakage current density of  $\approx 10^{-4}$  up to  $10^{-3}$  A cm $^{-2}$ , which is attributed to the presence of pinholes (Figure 1e,i). Devices prepared with YMO annealed at 725–800 °C (hexagonal YMO with a secondary orthorhombic phase) exhibit current densities of the order of  $\approx 10^{-6}$  A cm $^{-2}$ . To investigate the resistive switching behavior of the devices, a positive voltage sweep (from 0 to 5 V) was applied to the pristine high resistance state devices. Above a given threshold voltage ( $V_{\text{Set}}$ ), the device switches to a low resistance state (LRS). This corresponds to the Set process. A compliance current of 500  $\mu$ A was applied to prevent an irreversible hard breakdown of the device. For the Reset process, a negative voltage sweep (from 0 to  $-1.5$  V) was performed causing a decrease of the current at the Reset voltage ( $V_{\text{Reset}}$ ) to switch the device from LRS to high resistance state (HRS).

Figure 3c shows the typical  $I$ – $V$  characteristics of the Al/YMO/Pt devices based on a film annealed at 800 °C (h-YMO rich). The devices exhibit a forming-free bipolar resistive switching. The Set and Reset voltages as well as the HRS and LRS resistance values (read at 50 mV) are shown for the different device dimensions in Figure 3d,e, respectively. Both  $V_{\text{Set}}$  ( $+1.71 \pm 0.36$  V) and  $V_{\text{Reset}}$  ( $-0.36 \pm 0.08$  V) are quite low and the  $R_{\text{OFF}}/R_{\text{ON}}$  ratio is large, of the order of  $10^3$ – $10^4$ . In LRS, there is no dependence of the resistance on the device dimensions; hence the resistive switching is likely to occur through the formation of conductive filaments rather than through an interfacial mechanism where carriers are distributed along an interface.<sup>[36]</sup> The large variability of HRS values and the absence of dependence on the device dimension are consistent with the high resistance state originating from a partial rupture of the filaments during the switching from LRS to HRS. The retention for these devices, shown in Figure 3f, is of more than  $6 \times 10^3$  s with no drift in the ON and OFF states.

The devices prepared with YMO annealed at 900 °C shows electroforming-free bipolar RS with  $V_{\text{Set}}$  of  $+0.98 \pm 0.19$  V and  $V_{\text{Reset}}$  of  $-0.44 \pm 0.22$  V (Figure S7, Supporting Information). However, their endurance is quite poor; the devices remain in a conducting LRS after a few switching cycles and do not reset anymore. It is likely related to the presence of pinholes. Devices with amorphous YMO do not show resistive switching behavior but remain in the high resistance state or show a single irreversible breakdown. This observation suggests

that crystalline grain boundaries and/or boundaries between h-YMO and o-YMO are responsible for the resistive switching behavior in the polycrystalline films.

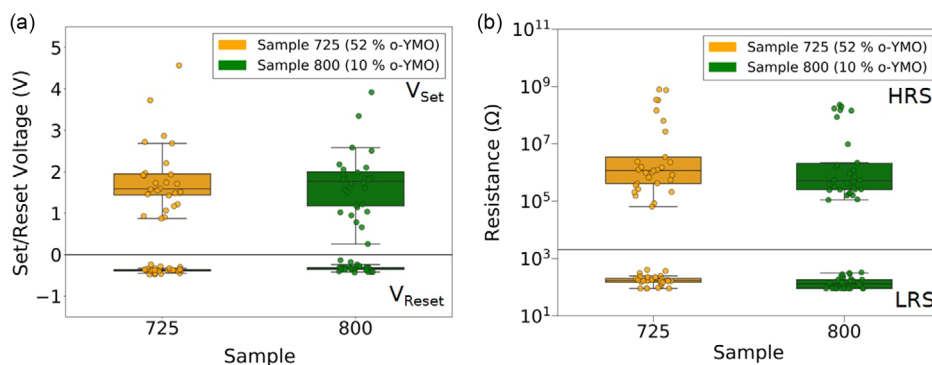
We compare in Figure 4 the switching characteristics of the devices with different amounts of secondary o-YMO phase, which both exhibit similar leakage current densities in the pristine state (Figure 2b). The Set and Reset voltages, the high and low resistances (determined at 50 mV) and the retention (shown in Figure S8, Supporting Information) are similar for both types of devices. Hence, no significant impact of the crystalline phase ratio is found on the macroscopic device resistive switching.

### 2.3. Thickness Effect

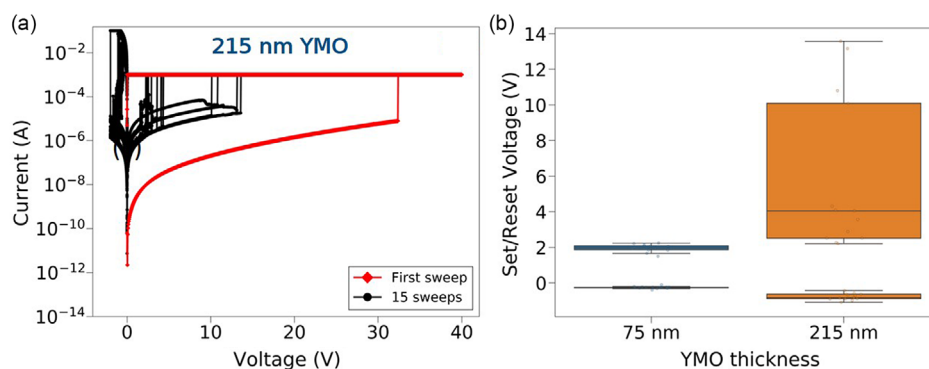
Figure 5a shows  $I$ – $V$  characteristics of an Al/YMO/Pt device with 215 nm-thick YMO film. The device requires a forming step with a high voltage of more than 30 V. The Set and Reset voltage dependence on YMO film thickness is presented in Figure 5b. For thicker YMO, the device shows a larger Set voltage, which reflects that the electric field drops with film thickness for a given voltage. The increase in  $V_{\text{Set}}$  scales with the increase in thickness (75–215 nm). The large variability observed for  $V_{\text{Set}}$  is coherent with the stochasticity of a filament growing along multiple grain boundaries throughout a thicker film. To minimize  $V_{\text{Set}}$ ,  $V_{\text{Reset}}$  and their variabilities, the thickness of 75 nm is preferred. It is a trade-off between the need to have a thick film to potentially develop many ferroelectric domains (for future co-development based on the combination of resistive switching and ferroelectricity) and the consideration of operational Set voltage and stochasticity, which increase with film thickness.

Table 3 summarizes the reports on the polycrystalline YMO-based resistive switching devices. Note that all these devices were prepared using pulsed laser deposition for YMO growth. We show in this work resistive switching behavior with the lowest operation voltages (both Set and Reset voltages) using RF sputtered YMO thin films.

The abruptness of the Set and Reset operations and the high ON/OFF resistance ratio point toward a filamentary mechanism. In the following, we discuss electrochemical metallization (ECM) as the mechanism at the origin of the resistive switching in our devices.



**Figure 4.** Variations of Set, Reset voltages a) and resistances in the low (LRS) and high (HRS) resistance states b) of devices fabricated with films annealed at 725 and 800 °C (read voltage of 50 mV). Median values and their corresponding median absolute deviations are represented.



**Figure 5.** a) Typical  $I$ - $V$  curves (15 cycles are shown) of Al/YMO/Pt devices with 215 nm-thick YMO film. The  $I$ - $V$  curve shown in red represents the first cycle (forming step). b) Variations of Set and Reset voltages of Al/YMO/Pt devices with 75 and 215 nm-thick YMO films.

## 2.4. Discussion on the Filamentary Mechanism

An ECM memristive device relies on the redox reactions of the active electrode and ion movement in the solid electrolyte, which leads to the formation of a metallic filament (Set operation) on the passive electrode giving rise to a low resistance state (LRS) when it bridges both electrodes.<sup>[37,38]</sup> The redox reactions are reversible and therefore the filament can be ruptured (Reset operation), leading back to a high resistance state (HRS).

Figure 6a shows the first positive voltage sweeps (from 0 to +5 V back to 0) for devices that did not switch under 5 V. All the  $I$ - $V$  curves, independently from the device area, show a current peak located at around 1.7 V, which hints to an electro-chemical metallization origin of the resistive switching in our devices. Indeed, Al can be oxidized to  $\text{Al}^{3+}$  at around 1.676 V.<sup>[39]</sup> The subsequent cycles do not show such a peak (Figure 6b) which is assigned to the irreversible oxidation of Al leading to the formation of  $\text{Al}_2\text{O}_3$  (hence the absence of switching in these devices). Cyclic voltammograms performed at different sweep rates (first cycle on several pristine devices) are shown in Figure 6c. The increase in total current and the shift of the redox potential toward larger positive values with increasing sweeping rates is in good agreement with a redox behavior.

To further clarify the role of Al electrodes, Pt/YMO/Pt devices were studied using the same  $I$ - $V$  measurement procedure (the voltage is applied from 0 to 5 or 10 V, with a sweep rate of  $75 \text{ mV s}^{-1}$  for the Forming/Set processes). A distinct behavior is clearly observed as compared to Al/YMO/Pt devices, as shown in Figure 7. In the range  $\pm 5 \text{ V}$ , there is no resistive switching. In all devices measured, a resistive switching is observed when a large Forming voltage of  $\approx 9 \text{ V}$  is applied. Given Pt's inert nature, no redox process is expected, and the YMO/Pt Schottky barrier is significantly lower than that of YMO/Al (more details will be discussed in Figure S9, Supporting Information), resulting in markedly larger leakage currents. A filamentary resistive switching is likely (due to the abruptness of the Set process), which stochastically requires Set voltages ranging from  $\approx 0.5$  to 8.4 V. The switching mechanism may be driven in this case by the formation/motion of defects already present in the active layer. However, the switching mechanism is clearly different for the devices with the Al top electrode and therefore we exclude in this

latter case a switching mechanism mainly driven by the formation/motion of defects in the polycrystalline film but conclude on an ECM type mechanism.

As a positive bias voltage is applied, the active electrode Al is oxidized (at  $V_{\text{Set}} = 1.7 \text{ V}$ ) and  $\text{Al}^{3+}$  metal cations move towards the inert Pt electrode under the applied electric field. When they reach the surface of the Pt electrode they are reduced and form an Al filament. The Al filament grows by the reduction of the subsequent  $\text{Al}^{3+}$  cations reaching it. Oppositely, the Al filaments can be ruptured by dissolution of Al in the film when a negative bias voltage is applied with Joule heating effects. Cu and Ag metals are most commonly used for the active electrode in ECM devices.<sup>[40-46]</sup> Due to its high oxygen affinity, when Al is used together with an amorphous electrolyte such as  $\text{SiO}_2$ , it forms a passive stable  $\text{Al}_2\text{O}_3$  barrier that reduces the current and subsequent further oxidation as shown by Luebbens et al.<sup>[47]</sup> The Al oxidation is irreversible i.e., oxidized Al cannot return to the metallic state thus precluding Set/Reset operations.<sup>[47]</sup> This is why there are no ECM resistive switching cells combining Al and  $\text{SiO}_2$  and more generally, no ECM resistive switching cells combining Al and an amorphous oxide, to the best of our knowledge. In our switched devices,  $\text{Al}^{3+}$  ions migrate most likely along oxygen-deficient defect lines such as grain boundaries so that the reversible formation of Al/ $\text{Al}^{3+}$  (and not  $\text{Al}_2\text{O}_3$ ) can occur. While most devices with YMO annealed at 725 and 800 °C switch to a highly conducting state at a Set voltage of  $1.7 \pm 0.36 \text{ V}$  (as shown in Figure 3 and 4), some do not (Figure 6a), which can be explained by the probable oxidation of Al to  $\text{Al}_2\text{O}_3$  upon  $\text{Al}^{3+}$  cation formation at 1.7 V. This might happen if a percolation path throughout the grain boundaries is not available.

For the switching devices, the electric field at Set voltage drives the migration of the  $\text{Al}^{3+}$  ions to the bottom inert electrode where reduction and nucleation/growth of the Al filament occurs. Several reports in literature show that there is no need for a large electric field for these processes to happen. For Cu electrodes and dense 10 nm  $\text{SiO}_2$  films, ultralow voltages of 250–400 mV were reported.<sup>[38,44]</sup> Moreover, specific microstructures and defect configurations within the electrolyte can significantly impact the ECM switching behavior. For instance, ECM cells based on Ag/280 nm  $\text{SiO}_2$ /ITO show a low switching

**Table 3.** Comparison of resistive switching performances and parameters of polycrystalline YMO-based resistive switching devices.

System	Switching mode	Film thickness [nm]	Film preparation	$V_{\text{Forming}}$ [V]	$V_{\text{Set}}$ [V]	$V_{\text{Reset}}$ [V]	ON/OFF	Retention [s]	Mechanism	References
Al/YMnO <sub>3</sub> /Pt	Bipolar	75	RF sputtering at RT, post-deposition annealing (725–800 °C)	Free	$\approx +1.71$ $\pm 0.36$	$\approx -0.36$ $\pm 0.08$	$\approx 10^4$	$> 6 \times 10^3$	Red/Ox metallic filament formation (Al)	This work
Pt/YMn <sub>1-<math>\delta</math></sub> O <sub>3</sub> /Pt	Unipolar	150	PLD at 800 °C	$\approx \pm 10$	$\approx \pm (2.2-10)$	$\approx \pm (0.6-1.3)$	$> 10^4$	$> 10^5$	Red/Ox metallic filament formation (Mn vacancy)	[5]
Au/YMnO <sub>3</sub> /Pt/Ti	Unipolar	150	PLD at 800 °C	Free	$\approx \pm 15$	$\approx \pm 2$	$> 10^3$	$> 5 \times 10^4$	Red/Ox metallic filament formation (oxygen vacancy)	[6]
Al/YMnO <sub>3</sub> /Pt/Ti	Unipolar	153	PLD at 800 °C	Free	$\approx \pm (3-20)$	$\approx \pm (0.7-5)$	$> 10^4$	$> 8 \times 10^4$	Red/Ox metallic filament formation (oxygen vacancy)	[7]
Al/YMnO <sub>3</sub> /Pt		189		Free (-), +20 (+)	$\approx -(3-20)$ , $+ (3-10)$					
Al/Y <sub>0.95</sub> Mn <sub>1.05</sub> /Pt	Unipolar	200	PLD at 800 °C	$\approx \pm 30$	$\approx \pm 10$	$\approx \pm 2$	$5.5 \times 10^5$	$> 8 \times 10^4$	Red/Ox metallic filament formation (oxygen vacancy)	[9]
Al/Y <sub>1</sub> Mn <sub>0.99</sub> Ti <sub>0.01</sub> /Pt				$\approx \pm 30$	$\approx \pm 20$	$5.0 \times 10^5$				
Al/Y <sub>0.94</sub> Mn <sub>1.05</sub> Ti <sub>0.01</sub> /Pt				Free	$\approx \pm 25$	$6.0 \times 10^5$				
In/YMnO <sub>3</sub> /NSTO	Bipolar	350	PLD at 800 °C	Free	+3.5	-3.5	$> 10^3$	$> 5 \times 10^4$	Polarization reversal-induced modification of the width of the depletion region at the p-n interface	[8]
Ag/Y <sub>0.95</sub> Sr <sub>0.05</sub> MnO <sub>3</sub> /Si	Bipolar	100	PLD at 700 °C	Free	+6	-6	3	-	Oxygen vacancy migration	[10]
Ag/Y <sub>0.95</sub> Ca <sub>0.05</sub> MnO <sub>3</sub> /Si	Bipolar	100	PLD at 700 °C	Free	+5	-5	$> 10^2$	-	Red/Ox metallic filament formation (oxygen vacancy)	[55]
Ag/Y <sub>0.95</sub> Ca <sub>0.05</sub> MnO <sub>3</sub> /NSTO	Unipolar	100	PLD at 700 °C	Free	$\pm 10$	$\pm 10$	$\approx 10$	$> 10^5$	Defects such as oxygen vacancy migration and charge trapping/detrapping at p-n interface	[56]

voltage of 0.2 V due to metallic Ag filaments growing in the nano-channels of porous SiO<sub>2</sub> film.<sup>[48]</sup>

In our devices, grain boundaries act as migration channels for the Al<sup>3+</sup> ions. Moreover, the quite large roughness of the YMO polycrystalline films might contribute to the relatively low operating voltage by favoring shorter migration paths (where the electric field is the largest)/preferred nucleation locations.

With high resistance values in HRS, high OFF/ON resistance ratio, abrupt Set/Reset, the dependence of the Set voltages on the film thickness, no switching occurring under the reverse bias, the evidence of a Set voltage that corresponds to the potential of Al oxidation, and the comparison with Pt top electrode, we can confidently assess the switching mechanisms to the ECM type.<sup>[47]</sup>

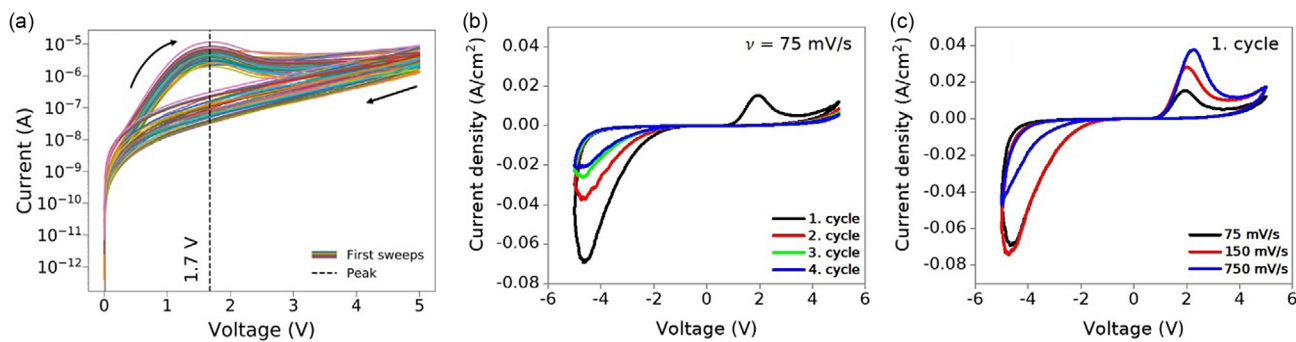


**Figure 6.** a) First positive voltage sweep (0 to +5 V to 0) of several Al/YMO/Pt devices that cannot be formed under 5 V, with different dimensions in sample 800 (film annealed at 800 °C). b) Cyclic voltammograms of Al/YMO/Pt for 4 cycles using a sweep rate of 75 mV s<sup>-1</sup>. c) Cyclic voltammograms of Al/YMO/Pt using different sweep rates. The YMO films used for all devices are 75 nm-thick.

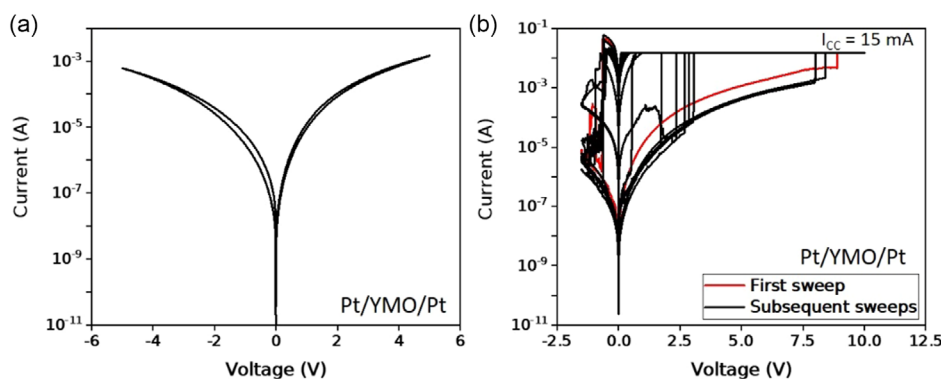


**Figure 7.** *I*-*V* characteristics of Pt/75 nm YMO/Pt devices with a) voltage sweep of 0 to 5 V to 0 and -5 V to 0 and b) voltage sweeps of 0 to 10 V to 0 to -1.5 V to 0. The sweep rate is 75 mV s<sup>-1</sup>. In (b), the Forming voltage is of 8.9 V. Set voltages vary between 0.5 and 8.4 V. Cycles #4 and #8 require a large Set voltage of 8.4 and 8.0 V respectively.

To further investigate the role of the YMO phases and of their boundaries in the formation of Al filament, the resistive switching behavior of the pure hexagonal or orthorhombic YMO phases were investigated using microscopic Al electrodes ( $\approx 1.5 \mu\text{m}$  diameter) patterned locally on each of the two phases on the film annealed at 725 °C. Local conductance mapping and local *I*-*V* measurements were performed on the bare surface and on the Al electrodes using c-AFM, as illustrated in Figure 8a. During the measurements, the cantilever tip was grounded, and the DC bias was applied to the bottom electrode. The compliance current was set to 100 nA. Since both h-YMO and o-YMO are p-type semiconductors,<sup>[34,49]</sup> the metal-semiconductor-metal structures can be regarded as back-to-back Schottky diodes. Both symmetric back-to-back Schottky diode structures (Pt coated tip/YMO/Pt) and asymmetric ones (Al/YMO/Pt) were measured as schematically shown in Figure 8b. Topography and c-AFM current maps are shown in Figure 8c,d respectively (Al top electrodes are marked with white circles). From the Raman spectroscopy discussed previously, the highly/lowly conductive regions in the film correspond to orthorhombic/hexagonal phases, respectively. No conduction is observed on the locations where the Al electrodes are positioned in the o-phase regions, which is confirmed also in the *I*-*V* measurements shown in Figure 8e. This can be explained by low leakage currents

resulting from the Al/o-YMO Schottky barrier, which is much higher than the Pt/o-YMO one and cannot be crossed easily by holes (h<sup>+</sup>) (see more detailed explanation in Figure S9, Supporting Information). We explored the resistive switching behavior of the micrometric-size Al/YMO/Pt devices on single h-YMO or o-YMO (Figure 8f). For comparison, we measured in the same conditions a  $100 \times 100 \mu\text{m}^2$  device as discussed in the previous section (such a large device comprises mixed hexagonal and orthorhombic YMO phases). For the large device ( $100 \times 100 \mu\text{m}^2$ ) an abrupt increase of current at a Set voltage of 4.6 V is observed, meaning that the resistive switching occurs. For the microscopic devices (at locations III and IV of Figure 8c,d), there is no change in current observed - hence no resistive switching behavior - for voltages up to 15 V. The grain size is of  $40 \pm 15 \text{ nm}$ , which means that the microscopic devices contain at least about 30–40 grains of the same phase. These observations indicate that the Al diffusion and filament formation likely happen along the boundaries between the orthorhombic and hexagonal phases (absent in the microscopic devices prepared in pure single phase) rather than along the grain boundaries between adjacent grains of a same given phase. Further work is needed to unveil details at the nanoscale on the switching mechanism(s).

The local c-AFM study clearly emphasizes the role of the mixed orthorhombic/hexagonal YMO phase boundaries in the

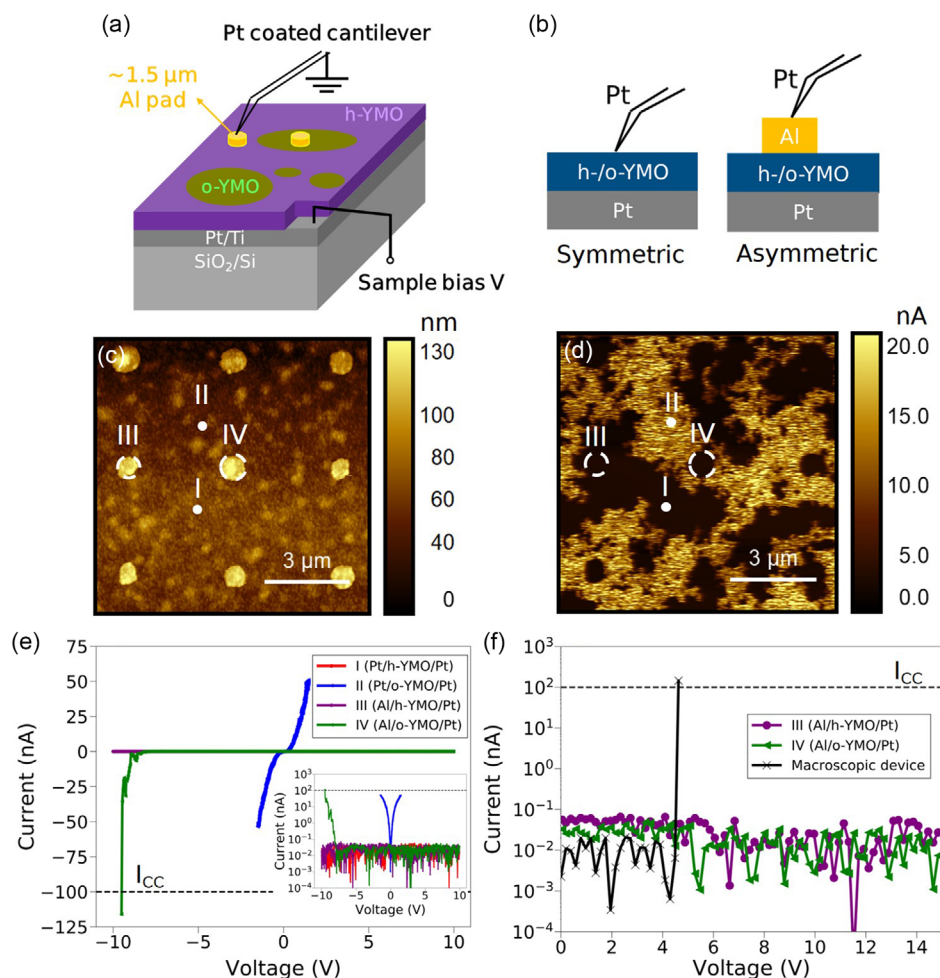


**Figure 8.** a) Sketch of the devices with Al top electrodes (diameter of 1.5  $\mu\text{m}$  and thickness of 60 nm) deposited locally in regions of pure h-YMO and pure o-YMO for c-AFM measurements. The cantilever was grounded, and the DC bias was applied to the sample bottom electrode. b) Sketches of the two types of stacks under study: Pt tip/h-(o-) YMO/Pt and Al/h-(o-) YMO/Pt. c) Topography and d) current maps measured with a DC bias of 1 V. White circles represent locations of the Al top electrodes. e)  $I$ - $V$  curves measured at four different locations (I and II: the tip was directly positioned on the film, III and IV: the tip was positioned on Al top electrodes). The tip DC bias (relative to sample bias) was: 0 to 10 V to 0 to  $-10$  V to 0 and the compliance current was 100 nA. The  $I$ - $V$  curves in semi-logarithmic scale are shown in the inset. f)  $I$ - $V$  characteristic of micro device III and IV (marked in panel d), with tip bias (relative to sample bias) 0 to 15 V. In addition,  $I$ - $V$  measurements with tip bias (from 0 to 5 V) on a macroscopic device ( $100 \times 100 \mu\text{m}^2$ ) was performed for comparison. The compliance current is 100 nA.

functionality of the devices. While, to the best of our knowledge, Al active electrode has never been reported in an ECM cell, we show here that engineering oxygen-deficient paths in the oxide electrolyte allows the electrochemical redox reactions to occur and the  $\text{Al}^{3+}$  cations to play an active role for the ECM operation.

### 3. Conclusion

Mixed hexagonal/orthorhombic polycrystalline  $\text{YMnO}_3$  films were synthesized by room temperature RF sputtering and post-deposition annealing in  $\text{N}_2$  atmosphere at 725–800  $^\circ\text{C}$ . While X-ray diffraction does not allow to unambiguously discriminate between orthorhombic and hexagonal phases, we show that the use of combined spectroscopies and microscopies

(Raman spectroscopy, SEM and even optical microscopy) does allow such identification. This study might trigger in the future more systematic investigations on the possible coexistence of polymorphs in polycrystalline  $\text{YMnO}_3$  (and more generally  $\text{RMnO}_3$  films) as the coexistence of phases may have a strong implication on the physical properties of the films. The unique microstructure of the mixed hexagonal/orthorhombic polycrystalline  $\text{YMnO}_3$  was used to develop electrochemical metallization memristive devices with Al active electrode. These devices show an electroforming-free bipolar resistive switching with a high  $R_{\text{OFF}}/R_{\text{ON}}$  ratio of  $10^4$ , low Set (1.7 V) and Reset ( $-0.36$  V) voltages and good retention performance. The origin of resistive switching is ascribed to the formation of an Al filament by electrochemical metallization upon positive voltage, which leads to an abrupt Set operation to a low resistance state and which

can be ruptured by application of a negative voltage back to a high resistance state. The absence of resistive switching behavior in the devices with single phase YMO (whether orthorhombic or hexagonal) points to the central role of the boundaries between the two crystalline phases for the diffusion of  $\text{Al}^{3+}$  ions in the YMO film. Hence, engineering oxygen-deficient paths via phase boundaries in a poly- nano-crystalline oxide electrolyte provides nanochannels for  $\text{Al}^{3+}$  migration and makes it possible to use Al as an active electrode. The localization/control of the migration of cations on the nanoscale level is a highly interesting approach for ECM cells as it removes a large part of the randomness of the migration of the metal cations from the active metal in the electrolyte.<sup>[50]</sup> More work is needed in the future to study the mechanisms and their dynamics at the nanoscale in these phase boundary channels with method such as operando transmission electron microscopy (TEM).<sup>[51]</sup>

This work opens up the perspective of designing, using a top-down approach, ultra-small nanoscale ECM cells based on the boundaries between two crystalline phases.

## 4. Experimental Section

**Thin Film Preparation and Characterization:** Polycrystalline YMO films (thickness of 75 and 215 nm) were synthesized on Pt 200 nm/Ti 30 nm/ $\text{SiO}_2/\text{Si}$  (001) substrates at room temperature by RF sputtering in an Ar atmosphere using a RF power of 200 W and an Ar pressure of 10  $\mu\text{bar}$ . The Pt/Ti-coated  $\text{SiO}_2/\text{Si}$  substrates were prepared by electron beam evaporation. The films were annealed after deposition for 30 min in a quartz tube furnace under 1 atm  $\text{N}_2$  at different temperatures (725, 800 and 900 °C). An amorphous YMO film was also investigated as a reference. Grazing incidence X-ray diffraction (GIXRD) performed on a Panalytical MPD diffractometer was used to identify the crystalline structures of YMO (fixed incident angle of  $\omega = 1^\circ$ ). The different phases were also studied locally by confocal Raman spectroscopy (Horiba LabRam) using a 325 nm laser in backscatter configuration. The surface morphology was characterized by SEM at 10.0 kV acceleration voltage (ZEISS-Gemini) and at 1.0 kV acceleration voltage (ZEISS-Merlin).

**Device Fabrication:** Metal/Insulating/Metal capacitors Al/YMO/Pt were fabricated with  $\approx 500$  nm-thick Al top electrodes by lift-off using photolithography and electron-beam evaporation. Different active device areas were investigated, from  $1.12 \times 10^{-4}$  to  $11.00 \times 10^{-4}$   $\text{cm}^2$  (overlapping of the top square electrode with the full sheet bottom electrode). Pt/YMO/Pt devices were fabricated with  $\approx 100$  nm-thick Pt top electrodes by lift-off using direct laser lithography (DLW66 + Heidelberg) and DC sputtering. In addition, for the characterization of single crystalline phase regions by conductive atomic force microscopy, small circular  $\approx 60$  nm-thick Al top electrodes of diameter 1.5  $\mu\text{m}$  were patterned by lift-off on the samples annealed at 725 °C by direct laser lithography (DLW66 + Heidelberg) and thermal evaporation.

**Electrical Measurements:** Current-voltage ( $I$ - $V$ ) measurements were performed on the Al/YMO/Pt and Pt/YMO/Pt devices at room temperature with a sweep speed of 75  $\text{mV s}^{-1}$  using a semiconductor parameter analyzer (Keysight B1500) and a probe station (MPI TS2000-SE). The Pt bottom electrode was grounded, and a DC bias was applied to the Al or Pt top electrode. A compliance current was set to 500  $\mu\text{A}$  (15 mA for Pt/YMO/Pt devices) to prevent an irreversible hard breakdown of the device. A positive voltage sweep (from 0 to typically 5 V) was applied, leading to a drastic increase of the current at the Set voltage ( $V_{\text{Set}}$ ); the device transitions from the high resistance state (HRS) to the low resistance state (LRS). For the first cycle, if the devices could not be switched under 5 V, a higher range (from 0 to 10 V) was used. Then, a negative voltage sweep (from 0 to  $-1.5$  V) was performed causing a decrease of the current at the Reset voltage ( $V_{\text{Reset}}$ ) to switch the device from LRS to HRS. The resistance in HRS

and LRS were determined from the  $I$ - $V$  characteristics with a readout voltage of 50 mV.

Conductive atomic force microscopy (c-AFM) mapped the local conductance of the films using a Park Systems NX10 microscope. The AFM tip (Nano sensors PPP-EFM) was grounded, and a DC bias was applied to the sample bottom electrode.

## Supporting Information

Supporting Information is available from the Wiley Online Library or from the author.

## Acknowledgements

The authors acknowledge funding of this work by the BMBF in the framework of the For-Mikro project ERMI (Erforschung rekonfigurierbarer, passiver Mikroelektronikbauelemente für Energieeffizienz und Flexibilität). The authors acknowledge the cooperation and funding of Park Systems for the study by AFM and c-AFM. The authors acknowledge the Center for Correlated Microscopy and Spectroscopy (CCMS) at HZB.

## Conflict of Interest

The authors declare no conflict of interest.

## Data Availability Statement

The data that support the findings of this study are available from the corresponding author upon reasonable request.

## Keywords

bipolar resistive switching, crystalline phase coexistence, electrochemical metallization, memristive device, polycrystalline  $\text{YMnO}_3$ , structure-physical properties, thin film

Received: November 19, 2023

Revised: January 18, 2024

Published online: February 2, 2024

- [1] H. L. Yakel Jnr, W. C. Koehler, E. F. Bertaut, E. F. Forrat, *Acta Crystallogr.* **1963**, *16*, 957.
- [2] M. Fiebig, D. Fröhlich, K. Kohn, S. Leute, T. Lottermoser, V. V. Pavlov, R. V. Pisarev, *Phys. Rev. Lett.* **2000**, *84*, 5620.
- [3] T. Choi, Y. Horibe, H. T. Yi, Y. J. Choi, W. Wu, S. W. Cheong, *Nat. Mater.* **2010**, *9*, 253.
- [4] T. Jungk, Á. Hoffmann, M. Fiebig, E. Soergel, *Appl. Phys. Lett.* **2010**, *97*, 012904.
- [5] Z. B. Yan, S. Z. Li, K. F. Wang, J. M. Liu, *Appl. Phys. Lett.* **2010**, *96*, 012103.
- [6] A. Bogusz, A. D. Müller, D. Blaschke, I. Skorupa, D. Bürger, A. Scholz, O. G. Schmidt, H. Schmidt, *AIP Adv.* **2014**, *4*, 107135.
- [7] V. R. Rayapati, N. Du, D. Bürger, R. Patra, I. Skorupa, P. Matthes, H. Stöcker, S. E. Schulz, H. Schmidt, *J. Appl. Phys.* **2018**, *124*, 144102.
- [8] L. Wei, C. H. Jia, W. F. Zhang, *RSC Adv.* **2016**, *6*, 1445.
- [9] V. R. Rayapati, D. Bürger, N. Du, R. Patra, I. Skorupa, D. Blaschke, H. Stöcker, P. Matthes, S. E. Schulz, H. Schmidt, *J. Appl. Phys.* **2019**, *126*, 074102.

- [10] K. N. Rathod, K. Gadani, H. Boricha, K. Sagapariya, A. Vaisnani, D. Dhruv, A. D. Joshi, J. P. Singh, K. H. Chae, K. Asokan, P. S. Solanki, N. A. Shah, *Phys. Status Solidi A* **2019**, 216, 1900780.
- [11] N. Fujimura, H. Tanaka, H. Kitahata, K. Tadanaga, T. Yoshimura, T. I. T. Ito, T. M. T. Minami, *Jpn. J. Appl. Phys.* **1997**, 36, L1601.
- [12] C. I. Cheon, K. Y. Yun, J. S. Kim, J. H. Kim, *Integr. Ferroelectr.* **2001**, 34, 73.
- [13] D. C. Yoo, J. Y. Lee, I. S. Kim, Y. T. Kim, *J. Cryst. Growth* **2001**, 233, 243.
- [14] I. Iliescu, M. Boudard, L. Rapenne, O. Chaix-Pluchery, H. Roussel, *Appl. Surf. Sci.* **2014**, 306, 27.
- [15] Y. Romaguera-Barcelay, J. A. Moreira, A. Almeida, P. B. Tavares, L. Fernandes, J. Pérez de la Cruz, *Ferroelectrics* **2016**, 498, 80.
- [16] R. Waser, R. Dittmann, C. Staikov, K. Szot, *Adv. Mater.* **2009**, 21, 2632.
- [17] a) E. Gebhardt, W. Köster, *Int. J. Mater. Res.* **1940**, 32, 253. b) ICDD:04-001-2680.
- [18] a) D. P. Kozlenko, S. E. Kichanov, S. Lee, J. G. Park, V. P. Glazkov, B. N. Savenko, *J. Exp. Theor. Phys. Lett.* **2005**, 82, 193; b) ICDD:04-011-9915.
- [19] a) V. E. Wood, A. E. Austin, E. W. Collings, K. C. Brog, *J. Phys. Chem. Solids* **1973**, 34, 859; b) ICDD:04-007-4495.
- [20] A. A. Bosak, C. Dubourdieu, J.-P. Sénateur, O. Y. Gorbenko, A. R. Kaul, *Cryst. Eng.* **2002**, 5, 355.
- [21] T. Atsumi, T. Ohgushi, N. Kamegashira, *J. Alloys Compd.* **1996**, 238, 35.
- [22] S. Ishiwata, Y. Tokunaga, Y. Taguchi, Y. Tokura, *J. Am. Chem. Soc.* **2011**, 133, 13818.
- [23] M. Počuča-Nešić, Z. Marinković Stanojević, Z. Branković, P. Cotič, S. Bernik, M. S. Góes, B. A. Marinković, J. A. Varela, G. Branković, *J. Alloys Compd.* **2013**, 552, 451.
- [24] A. Waintal, J. Chenavas, *Mater. Res. Bull.* **1967**, 2, 819.
- [25] K. Uusi-Esko, J. Malm, N. Imamura, H. Yamauchi, M. Karppinen, *Mater. Chem. Phys.* **2008**, 112, 1029.
- [26] G. Szabo, *Thèse Doctorat ès Sciences*, Lyon **1969**.
- [27] H. W. Brinks, H. Fjellvåg, A. Kjekshus, *J. Solid State Chem.* **1997**, 129, 334.
- [28] P. A. Salvador, T.-D. Doan, B. Mercey, B. Raveau, *Chem. Mater.* **1998**, 10, 2592.
- [29] A. A. Bosak, A. A. Kamenev, I. E. Graboy, S. V. Antonov, O. Y. Gorbenko, A. R. Kaul, C. Dubourdieu, J. P. Sénateur, V. L. Svechnikov, H. W. Zandbergen, B. Holländer, *Thin Solid Films* **2001**, 400, 149.
- [30] K. Bergum, H. Okamoto, H. Fjellvåg, T. Grande, M. A. Einarsrud, S. M. Selbach, *Dalton Trans.* **2011**, 40, 7583.
- [31] T. Ahmad, I. H. Lone, M. Ubaidullah, *RSC Adv.* **2015**, 5, 58065.
- [32] V. R. Rayapati, D. Bürger, N. Du, C. Kowol, D. Blaschke, H. Stöcker, P. Matthes, R. Patra, I. Skorupa, S. E. Schulz, H. Schmidt, *Nanotechnology* **2020**, 31, 31LT01.
- [33] A. Prikockytė, D. Bilc, P. Hermet, C. Dubourdieu, P. Ghosez, *Phys. Rev. B* **2011**, 84, 214301.
- [34] M. Sánchez-Pérez, O. J. Dura, J. P. Andrés, R. López Antón, J. A. Gonzalez, M. A. López De La Torre, *J. Appl. Phys.* **2019**, 126, 224103.
- [35] R. K. Kirby, *Int. J. Thermophys.* **1991**, 12, 679.
- [36] G. Sassine, S. La Barbera, N. Najjari, M. Minvielle, C. Dubourdieu, F. Alibart, *J. Vac. Sci. Technol., B: Nanotechnol. Microelectron.: Mater., Process., Meas., Phenom.* **2016**, 34, 012202.
- [37] I. Valov, R. Waser, J. R. Jameson, M. N. Kozicki, *Nanotechnology* **2011**, 22, 254003.
- [38] S. R. Nandakumar, M. Minvielle, S. Nagar, C. Dubourdieu, B. Rajendran, *Nano Lett.* **2016**, 16, 1602.
- [39] W. M. Haynes, D. R. Lide, T. J. Bruno, *CRC Handbook of Chemistry and Physics*, CRC Press, Boca Raton **2012**.
- [40] S. Tappertzshofen, H. Mündelein, I. Valov, R. Waser, *Nanoscale* **2012**, 4, 3040.
- [41] I. Valov, M. N. Kozicki, *J. Phys. D: Appl. Phys.* **2013**, 46, 074005.
- [42] I. Valov, E. Linn, S. Tappertzshofen, S. Schmelzer, J. Van Den Hurk, F. Lentz, R. Waser, *Nat. Commun.* **2013**, 4, 1771.
- [43] A. Mehonic, A. L. Shluger, D. Gao, I. Valov, E. Miranda, D. Ielmini, A. Bricalli, E. Ambrosi, C. Li, J. J. Yang, Q. Xia, A. J. Kenyon, *Adv. Mater.* **2018**, 30, 1801187.
- [44] F. Maudet, A. Hammud, M. Wollgarten, V. Deshpande, C. Dubourdieu, *Nanotechnology* **2023**, 34, 245203.
- [45] Z. Hu, F. Cao, T. Yan, L. Su, X. Fang, *J. Mater. Chem. C* **2023**, 11, 244.
- [46] F. Cao, Z. Hu, T. Yan, E. Hong, X. Deng, L. Wu, X. Fang, *Adv. Mater.* **2023**, 35, 2304550.
- [47] M. Lübben, I. Valov, *Adv. Electron. Mater.* **2019**, 5, 1800933.
- [48] J. Zhou, *Electron. Lett.* **2016**, 52, 965.
- [49] S. H. Skjærvø, E. T. Wefring, S. K. Nesdal, N. H. Gaukås, G. H. Olsen, J. Glaum, T. Tybell, S. M. Selbach, *Nat. Commun.* **2016**, 7, 13745.
- [50] M. J. Lee, S. Kim, S. Lee, C. Yoon, K. Min, H. Choi, S. Hong, S. Lee, J. Park, J. Ahn, B. H. Park, *NPG Asia Mater.* **2020**, 12, 82.
- [51] Y. Yang, P. Gao, L. Li, X. Pan, S. Tappertzshofen, S. Choi, R. Waser, I. Valov, W. D. Lu, *Nat. Commun.* **2014**, 5, 4232.
- [52] M. N. Iliev, H.-G. Lee, V. N. Popov, M. V. Abrashev, A. Hamed, R. L. Meng, C. W. Chu, *Phys. Rev. B* **1997**, 56, 2488.
- [53] M. N. Iliev, M. V. Abrashev, H. G. Lee, V. N. Popov, Y. Y. Sun, C. Thomsen, R. L. Meng, C. W. Chu, *J. Phys. Chem. Solids* **1998**, 59, 1982.
- [54] M. N. Iliev, M. V. Abrashev, H.-G. Lee, V. N. Popov, Y. Y. Sun, C. Thomsen, R. L. Meng, C. W. Chu, *Phys. Rev. B* **1998**, 57, 2872.
- [55] K. N. Rathod, K. Gadani, D. Dhruv, V. G. Shrimali, S. Solanki, A. D. Joshi, J. P. Singh, K. H. Chae, K. Asokan, P. S. Solanki, N. A. Shah, *J. Vac. Sci. Technol., B* **2020**, 38, 062208.
- [56] K. Gadani, K. N. Rathod, D. Dhruv, V. G. Shrimali, B. Rajyaguru, J. Joseph, A. D. Joshi, D. D. Pandya, K. Asokan, P. S. Solanki, N. A. Shah, *Mater. Sci. Semicond. Process.* **2021**, 121, 105347.